Supporting Information

Synergistic effects of chlorine substitution in sulfide electrolyte solid state battery

Eva Gil-González[1†], Luhan Ye[1†], Yichao Wang[1†], Zulipiya Shadike[2], Zhenming Xu[1], Enyuan Hu[2], and Xin Li[1*]

[1]John A. Paulson School of Engineering and Applied Sciences, Harvard University, Cambridge, MA 02138, USA
[2]Chemistry Division, Brookhaven National Laboratory, Upton, NY 11973, USA

[†] Equal Contribution
[*] Corresponding author: lixin@seas.harvard.edu

Materials and Methods

Sample preparation

$Li_{5.5}PS_{4.5}Cl_{1.5}$ (LPSCl1.5), $Li_6PS_5Cl_{1.0}$ (LPSCl1.0), $Li_{6.5}PS_{5.5}Cl_{0.5}$ (LPSCl0.5), and $Li_7P_3S_{11}$ (LPS) were prepared by mechanosynthesis and a post annealing treatment. For LPS stoichiometric amounts of Li_2S ((>99.9% purity, Alfa Aesar)) and P_2S_5 (S >99% purity, Sigma Aldrich) were milled for 10 hours. While for LPSCl, Li_2S ((>99.9% purity, Alfa Aesar)), P_2S_5 (S >99% purity, Sigma Aldrich) and LiCl (>99% purity, Alfa Aesar) were milled for 16 hours at 460 rpm. Both milling processes were carried out in a planetary mill PM200 (Retsch GmbH, Germany) under a protective Argon atmosphere to avoid the oxidation of the compounds. Subsequently, the mechanosynthesized powder was transferred to quartz tubes, which were sealed and heated at 550 ºC or 260 ºC for 8 hour for LPSCl and LPS, respectively.

Sample characterization

X-Ray Diffraction (XRD) patterns were collected in a Rigaku Miniflex 600 diffractometer (CuK_α radiation, $\lambda = 0.15405$ nm) working at 40 kV and 15 mA. Measurements were taken within a 2θ range from 15 to 80º, with a 0.02 º step and a scan speed of 0.24 seconds per step. Sample holders were sealed with Kapton film in Ar-filled glovebox to avoid the air exposure during measurements.

X-Ray Photoelectron Spectroscopy (XPS) data were taken in a Thermo Scientific K-Alpha+ with a beam size of 70 μm and at chamber pressure of approximately 10^{-7} Pa. The C 1s signal of adventitious carbon (285 eV) was used for charge correction and data fitting was performed using the Avantage software package. Extreme precautions were taken to protect and avoid the samples from the contact with air during the transfer from Ar-filled glovebox to XPS vacuum chamber.

XAS Characterization: Ex situ measurements of P K- and S K-edges were performed at the Advanced Photon Source on the bending-magnet beamline 9-BM-B with electron energy of 7 GeV and average current of 100 mA. The radiation was monochromatized by a Si (111) double-crystal monochromator. At the S K-edge, spectra were collected in fluorescence mode using a four-element vortex detector. All samples were measured in helium-filled chamber. The X-ray absorption near-edge structure (XANES) spectra were processed using the Athena software package[1].

Electrochemical characterization

The ionic conductivity of LPSCl and LPS was measured by Impedance Spectroscopy in a Solartron electrochemical potentiostat (1470E + 1455 FRA), over the frequency range from 100 Hz to 1 MHz, with AC measuring voltage of 0.01 V at room temperature (20 ºC). Cells with C-SE/SE/C-SE configuration were used, where a layer of solid electrolyte (SE) powder was sandwiched by two C-SE composite layers, which served as electrodes. The electrode composition is 90% of SE (w/w) and 10% of Carbon black (w/w), and the three-layered cells were cold pressed at 150 MPa prior the impedance measurement.

Asymmetric batteries, Li/SE/SS, where SE is either LPSCl or LPS and SS (Stainless Steel) is the current collector, were assembled to study the electrochemical compatibility of both solid electrolytes against Li metal as well as the effect of mechanical contrition. Cells were previously pressed at 125 MPa and then discharged at a current density of 0.25 mA cm^{-2} down to -1 V in a LANDT CT2001 battery test system. When the effect of mechanical constriction was being evaluated a pressure of 38 MPa was applied during the discharged.

Symmetric batteries Li/SE/Li (SE=LPSCl0.5, LPSCl1.0, LPSCl1.5, and their combinations) were tested in a LANDT CT2001 battery test system at a current density of 0.1 or 0.25 mA cm^{-2}, with continuous 1 h plating/stripping durations. In order to investigate the stability window of LPSCl, cyclic voltammograms (CV) tests of Li/LPSCl/LPSCl-C (cathode composition 0.9:0.1-LPSCl:Carbon black (w/w)) were collected on a Solartron 1455A with a voltage sweeping rate of 0.1 mV s^{-1} from 0.1 to 6 V. For the low voltage region, cells were scanned from Open Circuit Voltage (OCV) to 0.1 V and then back to 2.5 V. For the high voltage region, cells were tested from OCV to 6 V and subsequently scanned back to 2.5 V. All cells were previously pressed at 125 MPa and an external pressure of 38 MPa was applied during test. For comparison purposes, liquid cells were also tested under identical conditions from OCV to 3.2 V or 4.2 V. These cells were assembled in Swagelok cases with Li metal as the counter electrode, glass fiber as separator and commercially available liquid electrolyte, particularly $LiPF_6$ solution in ethylene carbonate and diethyl carbonate (1 M $LiPF_6$ in EC/DEC=50/50 (v/v), battery grade, Sigma Aldrich). Films of the same composition instead of powder were used as cathode. Thus, 3% extra of

polytetrafluoroethylene (PTFE) was employed to make those films, which were rolled and punched into discs of 5/16" diameter (1-2 mg of mass). The current densities obtained from CV tests for the different cells were normalized to 1 g of LPSCl, as all cells have the same area (1/2" diameter).

The galvanostatic battery cycling tests were performed on an Arbin BT2000 workstation. Two different battery configurations were used depending on the employed cathode materials: commercially available $LiCoO_2$ (LCO), $LiNi_{0.83}Mn_{0.06}Co_{0.11}O_2$ (NMC811), or $LiNi_{0.5}Mn_{1.5}O_4$ (LNMO) with the cathode loading of 2 mg/cm^2. The cathode was made with active material : SE: PTFE = 70:30:3 weight ratio. In the case of LCO, Li/SE/LCO (SE= LPSCl, LPS, LGPS) cells were assembled, where Li metal was directly used as anode material. Thus, ½'' diameter Li metal discs were directly pressed with 150 mg of SE powder, which were used as separator, and 5/16" diameter films of LCO (70:30-LCO:SE weight ratios, +3% extra of PTFE). The thickness of the solid electrolyte is ~500 µm after press. These three-layered cells were cold pressed at 125 MPa and an external pressure of 38 MPa was applied during test to prevent immediate short-circuit. The batteries were tested between 2.5 and 4.2 V at a charge-discharge C-rate of 0.1 at room temperature. When LNMO or NMC811 was used as active cathode material (film composition of 70:30-active material:SE weight ratios (SE= LPSCl, LPS or LGPS), +3% extra of PTFE), Li-g/SE/LNMO cells were assembled following the procedure described above. Analogously, Li-g/SE/LNMO batteries were pressed at 390 MPa and an external pressure of 77 MPa was applied during test. In this work, a small formation pressure was applied to the battery with pure Li to prevent its mechanical penetration, while a higher pressure was applied to the battery with graphite covered Li since graphite has the right mechanical property to prevent Li penetration. The capacity ratio between Li and graphite layer is 2.5, while the thicknesses of Li and graphite are 25 µm and 30 µm, respectively. LNMO Cells were charged and discharged at 0.1 C from 2.5 to 5.2 V at 55 ℃.

Computational simulation

Ab-initio molecular dynamics (AIMD) simulations were carried out by using the projector augmented wave method in the framework of the density functional theory (DFT),[3] as implemented in the Vienna *ab*-initio Simulation Package (VASP). The plane-wave energy cutoff was set to 300 eV, and the Γ-centered 1 × 1 × 1 k-point mesh method was employed for the Brillouin zone sampling. All AIMD calculations were performed without spin-polarization in an NVT canonical ensemble at elevated temperatures with a Nose−Hoover thermostat.[4] The total time for each AIMD simulation was 100 ps, with 2 fs as time step. The simulation supercell sizes were at least 10 Å along each lattice direction. The Li ion diffusion coefficients of each temperature-dependent AIMD simulation were obtained from a linear fit of the mean square

displacement (MSD) of Li ions with respect to time. Arrhenius plots were constructed from simulations at elevated temperatures to obtain the activation energy and extrapolated room-temperature self-diffusivity and conductivity.[5]

The stability voltage windows, hull energies and reaction strains of electrolytes and interphases under mechanical constriction were calculated using Lagrange minimization schemes as outlined by Fitzhugh et al. for effective moduli of 0, 10 and 20 GPa.[6] Interphase was created by pseudo phase method at the mixing ratio of 1:1, both phase energy and volume are interpolated. All phases with elements within the electrolyte's or interphase's elemental space were considered, except LiS_4 (mp-995393), SCl_3 (mp-1186934) and $Li_5PS_4Cl_2$ (mp-1040450) in the Materials Project database since they are neither likely to be in the decomposition product nor actually exist. $Li_5PS_4Cl_2$ (mp-1040450) was considered only when calculation is on itself. In the pseudo electronic resistance calculation by the circuit model, band gap values are acquired from the Materials Project database except Li_2PS_3. The recorded 0 eV band gap of Li_2PS_3 was recalculated to be 2.5 eV by DFT.

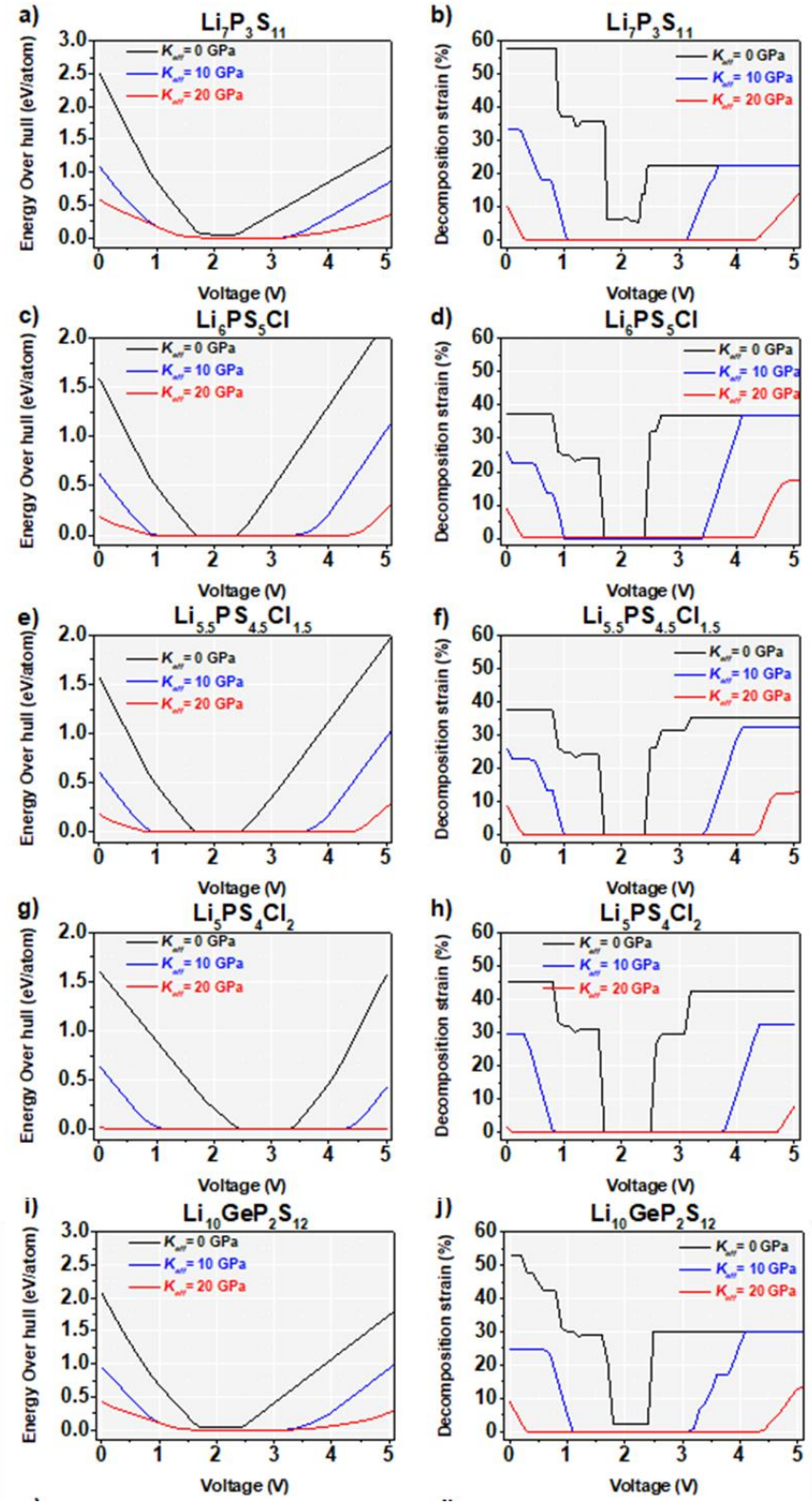

Figure S1. Decomposition energy and strain for $Li_7P_3S_{11}$ (a, b), Li_6PS_5Cl (c, d), $Li_{5.5}PS_{4.5}Cl_{1.5}$ (e, f), $Li_5PS_4Cl_2$ (g, h) and $Li_{10}GeP_2S_{12}$ (i, j) at different effective moduli K_{eff}, which is a metric for the level of local mechanical constrictions.

Table S1. $Li_{5.5}PS_{4.5}Cl_{1.5}$ decomposition products with fraction numbers within each voltage range at effective moduli K_{eff} = 0 and 20 GPa, which is a metric for the level of local mechanical constrictions. The pseudo-bandgap of the decomposition interphase is calculated by $\boldsymbol{E_g = \frac{\sum_i x_i n_i V_i E_g^i}{\sum_i x_i n_i V_i}}$, where for any decomposition product *i*, $\boldsymbol{V_i}$ is the molar volume per atom , $\boldsymbol{n_i}$ is the atomic number per formula, $\boldsymbol{x_i}$ is the pre-factor in the decomposition reaction equation, and $\boldsymbol{E_g^i}$ is the bandgap. $\boldsymbol{E_g^i}$ is in Table S4, while V_i can be converted from Table S4. The pseudo-resistivity of the decomposition interphase is calculated by the circuit model described in Figure S2.

$\boldsymbol{K_{eff} = 0GPa}$	**$Li_{5.5}PS_{4.5}Cl_{1.5}$+xLi (reactants)**	**Decomposition products**	**Interphase Pseudo-Bandgap (E_g)**	**Interphase Pseudo-resistivity (R)**
5.00V	$Li_{5.5}PS_{4.5}Cl_{1.5}$	0.077PCl_3+0.462P_2S_7+1.267 SCl+5.5Li	1.652	3.07E+00
3.20V	$Li_{5.5}PS_{4.5}Cl_{1.5}$	0.077PCl_3+0.462P_2S_7+1.267 SCl+5.5Li	1.652	3.07E+00
2.70V	$Li_{5.5}PS_{4.5}Cl_{1.5}$	0.496LiCl+0.496P_2S_7+1.001 SCl+5.005 Li	1.841	3.41E+00
2.50V	$Li_{5.5}PS_{4.5}Cl_{1.5}$	1.001S+1.498LiCl+0.496 P_2S_7+4.004Li	2.392	4.39E+00
2.40V	Stable	1.00 $Li_{5.5}PS_{4.5}Cl_{1.5}$	2.139	8.58E+35
1.70V	Stable	1.00 $Li_{5.5}PS_{4.5}Cl_{1.5}$	2.139	8.58E+35
1.30V	$Li_{5.5}PS_{4.5}Cl_{1.5}$+4.997 Li	1.001P+1.498 LiCl+4.501Li_2S	3.901	4.40E+59
1.20V	$Li_{5.5}PS_{4.5}Cl_{1.5}$+5.138 Li	0.14LiP_7+1.498LiCl+4.501 Li_2S	3.892	4.33E+59
1.00V	$Li_{5.5}PS_{4.5}Cl_{1.5}$+5.418 Li	0.14Li_3P_7+1.498LiCl+4.48L i_2S	3.876	4.46E+59
0.90V	$Li_{5.5}PS_{4.5}Cl_{1.5}$+5.999 Li	1.001LiP+1.498LiCl+4.501 Li_2S	3.760	4.56E+59
0.00V	$Li_{5.5}PS_{4.5}Cl_{1.5}$+8.001 Li	1.001Li_3P+1.498LiCl+4.501 Li_2S	3.532	5.60E+59

$\boldsymbol{K_{eff} = 20GPa}$	**$Li_{5.5}PS_{4.5}Cl_{1.5}$+ xLi (reactants)**	**Decomposition products**	**Interphase Pseudo-Bandgap (E_g)**	**Interphase Pseudo-resistivity (R)**
5.00V	$Li_{5.5}PS_{4.5}Cl_{1.5}$	1.127S+0.378SCl_4+1.001Li_2P S_3+3.5Li	1.916	4.70E+00
4.70V	$Li_{5.5}PS_{4.5}Cl_{1.5}$	1.127S+0.378SCl_4+1.001Li_2P S_3+3.5Li	1.916	4.70E+00
4.60V	$Li_{5.5}PS_{4.5}Cl_{1.5}$	0.986S+0.329SCl_4+0.875Li_2P S_3+0.063$Li_{5.5}PS_{4.5}Cl_{1.5}$+3.059 Li	1.940	5.19E+00
4.50V	$Li_{5.5}PS_{4.5}Cl_{1.5}$	0.581S+0.196SCl_4+0.518Li_2P S_3+0.238$Li_{5.5}PS_{4.5}Cl_{1.5}$+1.848 Li	2.017	2.28E+36
4.40V	$Li_{5.5}PS_{4.5}Cl_{1.5}$	0.175S+0.011P_2S_7+0.056SCl_4 +0.161$Li_{5.5}PS_{4.5}Cl_{1.5}$+0.56Li	2.100	1.10E+36
4.30V	Stable	1.00 $Li_{5.5}PS_{4.5}Cl_{1.5}$	2.139	8.58E+35
0.80V	Stable	1.00 $Li_{5.5}PS_{4.5}Cl_{1.5}$	3.723	2.54E+42
0.30V	$Li_{5.5}PS_{4.5}Cl_{1.5}$+ 1.26Li	1.498LiCl+1.722Li_2S+0.042P $_2S$+0.91Li_2PS_3	3.723	2.54E+42
0.20V	$Li_{5.5}PS_{4.5}Cl_{1.5}$+ 1.95Li	1.47LiCl+2.31Li_2S+0.16P_2S+ 0.68Li_2PS_3	3.734	3.22E+42

0.10V	$Li_{5.5}PS_{4.5}Cl_{1.5}$+ 1.75Li	1.498LiCl+2.128Li_2S+0.126P $_2S$+0.749Li_2PS_3	3.748	4.84E+42
0.00V	$Li_{5.5}PS_{4.5}Cl_{1.5}$+ 3.08Li	1.498LiCl+3.241Li_2S+0.350P $_2S$+0.301Li_2PS_3	3.760623956	5.46225E+59

Table S2. $Li_7P_3S_{11}$ decomposition products with fraction numbers within each voltage range at K_{eff} = 0 and 20 GPa, together with the pseudo-bandgap $\boldsymbol{E_g = \frac{\sum_i x_i n_i V_i E_g^i}{\sum_i x_i n_i V_i}}$ and the pseudo-resistivity of the decomposition interphase, following the circuit model in Figure S2.

$\boldsymbol{K_{eff} = 0GPa}$	**$Li_7P_3S_{11}$+xLi (reactants)**	**Decomposition products**	**Interphase Pseudo-Bandgap (E_g)**	**Interphase Pseudo-resistivity (R)**
5.00V	$Li_7P_3S_{11}$	0.504S+1.498P_2S_7+7.00Li	1.525	3.95E+00
2.50V	$Li_7P_3S_{11}$	0.504S+1.498P_2S_7+7.00Li	1.525	3.95E+00
2.40V	Stable	1.00$Li_7P_3S_{11}$	2.417	4.06E+40
1.80V	Stable	1.00$Li_7P_3S_{11}$	2.417	4.06E+40
1.7V	$Li_7P_3S_{11}$+15.008 Li	2.996P+11.004Li_2S	3.323	2.19E+59
1.3V	$Li_7P_3S_{11}$+15.12Li	2.996P+11.004Li_2S	3.323	2.19E+59
1.2V	$Li_7P_3S_{11}$+15.442 Li	0.434LiP_7+11.004Li_2S	3.303	2.22E+59
1.0V	$Li_7P_3S_{11}$+16.310 Li	0.434Li_3P_7+11.004Li_2S	3.290	2.17E+59
0.9V	$Li_7P_3S_{11}$+18.004 Li	2.996LiP+11.004Li_2S	3.123	2.12E+59
0V	$Li_7P_3S_{11}$+23.996 Li	2.996Li_3P+11.004Li_2S	2.869	9.73E+15

$\boldsymbol{K_{eff} = 20GPa}$	**$Li_7P_3S_{11}$+xLi (reactants)**	**Decomposition products**	**Interphase Pseudo-Bandgap (E_g)**	**Interphase Pseudo-resistivity (R)**
5.00V	$Li_7P_3S_{11}$	1.064S+0.938P_2S_7+1.12 Li_2PS_3+4760Li	1.802	5.56E+00
4.90V	$Li_7P_3S_{11}$	1.148S+0.84P_2S_7+1.302 Li_2PS_3+4.396Li	1.855	6.01E+00
4.80V	$Li_7P_3S_{11}$	1.246S+0.756P_2S_7+1.498Li_2PS_3+4.004Li	1.910	4.74E+34
4.70V	$Li_7P_3S_{11}$	1.344S+0.658P_2S_7+1.694Li_2PS_3+3.612Li	1.968	5.32E+34
4.60V	$Li_7P_3S_{11}$	1.442S+0.56P_2S_7+1.876 Li_2PS_3+3.248Li	2.027	6.09E+34
4.50V	$Li_7P_3S_{11}$	1.54S+0.462P_2S_7+2.072 Li_2PS_3+2.856Li	2.088	7.18E+34
4.40V	$Li_7P_3S_{11}$	1.638S+0.364P_2S_7+2.268Li_2PS_3+2.464Li	2.152	8.84E+34

3.90V	$Li_7P_3S_{11}$	1.638S+0.364P_2S_7+2.282Li_2PS_3+2.436Li	2.158	9.06E+34
3.70V	Stable	1.00 $Li_7P_3S_{11}$	2.417	4.06E+40
1.30V	Stable	1.00$Li_7P_3S_{11}$	2.417	4.06E+40
1.20V	$Li_7P_3S_{11}$+5.10Li	0.098LiP_5+3.5Li_2S+2.506Li_2PS_3	2.854	1.70E+42
0.30V	$Li_7P_3S_{11}$+5.43Li	4.018Li_2S+0.406P_2S+2.198Li_2PS_3	2.833	1.98E+42
0.20V	$Li_7P_3S_{11}$+6.3Li	4.746Li_2S+0.546P_2S+1.904Li_2PS_3	2.865	2.39E+42
0.10V	$Li_7P_3S_{11}$+7.50Li	5.754Li_2S+0.756P_2S+1.498Li_2PS_3	2.906	3.20E+42
0.00V	$Li_7P_3S_{11}$+8.70Li	6.762Li_2S+0.952P_2S+1.092Li_2PS_3	2.945	4.62E+42

Table S3. $Li_{10}GeP_2S_{12}$ decomposition products with fraction numbers within each voltage range at K_{eff} = 0 and 20 GPa, together with the pseudo-bandgap $\boldsymbol{E_g = \frac{\sum_i x_i n_i V_i E_g^i}{\sum_i x_i n_i V_i}}$ and the pseudo-resistivity of the decomposition interphase, following the circuit model in Figure S2.

decomposition interphase, following the circuit model in Figure S2.

$\boldsymbol{K_{eff} = 0GPa}$	**$Li_{10}GeP_2S_{12}$ +xLi (reactants)**	**Decomposition products**	**Interphase Pseudo-Bandgap (E_g)**	**Interphase Pseudo-resistivity (R)**
5.00	$Li_{10}GeP_2S_{12}$	10.005Li+3.0S+1.005P_2S_7+1.005GeS_2	1.546	4.06E+00
2.60	$Li_{10}GeP_2S_{12}$	10.005Li+3.0S+1.005P_2S_7+1.005GeS_2	1.546	4.06E+00
2.50	Stable	$Li_{10}GeP_2S_{12}$	2.364	5.25E+39
1.70	Stable	Li10Ge1P2S12	2.364	5.25E+39
1.60	$Li_{10}GeP_2S_{12}$ +13.995Li	13.995Li+1.995P+1.005Ge+12.0Li_2S	3.272	2.04E+59
1.20	$Li_{10}GeP_2S_{12}$ +14.28Li	1.005Ge+0.285LiP_7+12.0Li_2S	3.259	2.07E+59
0.50	$Li_{10}GeP_2S_{12}$ +20.985Li	1.995Li_3P+12.0Li_2S+1.005LiGe	2.933	1.69E+59
0.40	$Li_{10}GeP_2S_{12}$ +22.275Li	1.995Li_3P+12.0Li2S+0.255Li_9Ge_4	2.868	1.64E+59
0.20	$Li_{10}GeP_2S_{12}$ +23.805Li	1.995Li_3P+12.0Li_2S+0.255$Li_{15}Ge_4$	2.772	1.57E+59
0.00	$Li_{10}GeP_2S_{12}$ +23.805Li	1.995Li_3P+12.0Li_2S+0.255$Li_{15}Ge_4$	2.772	1.57E+59

$\boldsymbol{K_{eff} = 20GPa}$	**$Li_{10}GeP_2S_{12}$ +xLi (reactants)**	**Decomposition products**	**Interphase Pseudo-Bandgap (E_g)**	**Interphase Pseudo-resistivity (R)**
5.00	$Li_{10}GeP_2S_{12}$	6.015Li+4.005S+1.005GeS_2+1.995Li_2PS_3	1.985	5.60E+00

4.90	$Li_{10}GeP_2S_{12}$	5.3545Li+3.675S+0.84GeS$_2$+1.995Li$_2$PS$_3$+0.164Li$_4$GeS$_4$	2.036	5.71E+00
4.80	$Li_{10}GeP_2S_{12}$	4.575Li+3.285S+0.644GeS$_2$+1.995Li$_2$PS$_3$+0.36Li$_4$GeS$_4$	2.098	3.20E+42
4.70	$Li_{10}GeP_2S_{12}$	3.345Li+1.665S+0.345P$_2$S$_7$+1.319Li$_2$PS$_3$+1.005Li$_4$GeS$_4$	2.124	1.61E+42
4.60	$Li_{10}GeP_2S_{12}$	2.925Li+1.77S+0.224P$_2$S$_7$+1.529Li$_2$PS$_3$+1.005Li$_4$GeS$_4$	2.186	1.41E+42
4.50	$Li_{10}GeP_2S_{12}$	2.475Li+1.875S+0.12P$_2$S$_7$+1.755Li$_2$PS$_3$+1.005Li$_4$GeS$_4$	2.250	1.25E+42
4.40	$Li_{10}GeP_2S_{12}$	2.055Li+1.98S+0.015P$_2$S$_7$+1.965Li$_2$PS$_3$+1.005Li$_4$GeS$_4$	2.317	1.13E+42
4.30	$Li_{10}GeP_2S_{12}$	1.995Li+1.995S+1.995Li$_2$PS$_3$+1.005Li$_4$GeS$_4$	2.324	1.11E+42
4.10	Stable	$Li_{10}GeP_2S_{12}$	2.364	5.25E+39
1.10	Stable	$Li_{10}GeP_2S_{12}$	2.364	5.25E+39
1.00	$Li_{10}GeP_2S_{12}$+4.455 Li	5.324Li$_2$S+0.03GeP$_3$+0.96GeS+1.905Li$_2$PS$_3$	2.903	2.59E+42
0.20	$Li_{10}GeP_2S_{12}$+5.415 Li	6.0Li$_2$S+0.134GeP$_2$+0.855GeS+1.71Li$_2$PS$_3$	2.944	2.94E+42
0.10	$Li_{10}GeP_2S_{12}$+6.855 Li	7.38Li$_2$S+0.48P$_2$S+1.005GeS+1.05Li$_2$PS$_3$	2.969	5.09E+42
0.00	$Li_{10}GeP_2S_{12}$+8.205 Li	8.504Li$_2$S+0.705P$_2$S+1.005GeS+0.6Li$_2$PS$_3$	3.006	1.36E+59

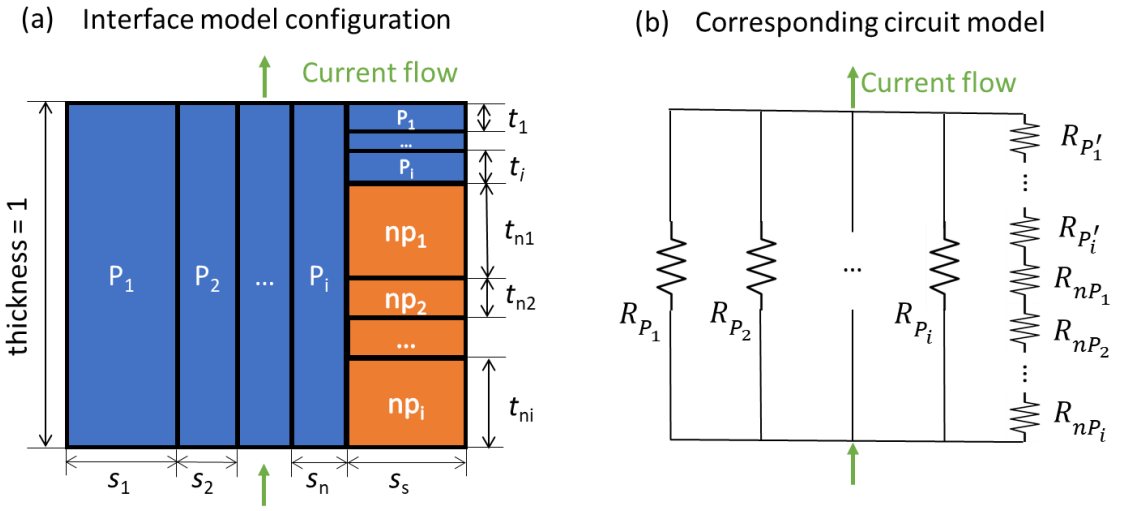

Figure S2. Circuit model for calculating pseudo electronic resistance of the decomposition interphase. **(a)** The interface model configuration: percolated decomposition products (P_i) are parallel to each other, and the non-percolated products (nP_i) are serial in another parallel branch

along with percolated products. The total volume fraction of P_i in the serial part is set as the average volume fraction of nP_i. The thickness of the interface is set to 1 and the volume fraction of each products determines the dimensionless area *s* and thickness *t*. **(b)** The corresponding circuit used to calculate the total pseudo-resistivity R of the decomposition interphase Based on Fig. S2a. Decomposition products with volume fraction larger than 0.183[7] threshold are considered as percolated and are labeled as P_i, while other non-percolated products (nP_i) are surrounded by percolated products, and thus are assigned to be connected in series. All dimensionless area *s* and thickness *t* can be calculated with the volume fraction given by the thermodynamic prediction in Table S1-S3. The pseudo resistivity R_{Pi} or R_{nPi} of each product is defined and calculated by $\exp\left(-\frac{E_g^i}{k_B T}\right) \times t/s$, where T = 300 K and E_g^i can be obtained from Table S4.

Table S4. Bandgap and molar volume per atom of decomposition products of $Li_7P_3S_{11}$ and $Li_{5.5}PS_{4.5}Cl_{1.5}$. x and √ represent low- and high-voltage decomposition products, respectively, beyond the voltage stability window at a given K_{eff}. **(e.g., Low voltage rage:** 0-1.7 V at 0 GPa and 0-0.8V at 20 GPa for $Li_{5.5}PS_{4.5}Cl_{1.5}$; 0-1.8 V at 0 GPa and 0-1.3V at 20 GPa for $Li_7P_3S_{11}$, **High voltage rage:** 2.4-5 V at 0 GPa and 4.3-5V at 20 GPa for $Li_{5.5}PS_{4.5}Cl_{1.5}$; 2.4-5 V at 0 GPa and 3.7-5 V at 20 GPa for $Li_7P_3S_{11}$)

Decomposition product	**Band Gap (E_g, eV)**	**Molar volume (V, Å^3)**	$Li_7P_3S_{11}$		$Li_{5.5}PS_{4.5}Cl_{1.5}$	
			$0GPa$	$20GPa$	$0GPa$	$20GPa$
Li_3P	0.9164	14.7	x		x	
Li_2S	3.538	15.6	x	x	x	x
LiP	0.853	15.7	x		x	
Li_3P_7	1.792	19.9	x		x	
LiP_7	1.656	21.5	x		x	
P	1.92	26.5	x		x	
P_4S_3	2.869	33.3	x			
P_4S_7	2.776	30.9	x			
Li_3PS_4	2.833	20.8	x	x		
P_2S_5	2.577	30.6	x			
P_2S_7	2.035	27.9	x	x	√	√
Li	0	20.1	√	√	√	√
S	2.740	36.0	√	√	√	√
P_2S*	0	16.2		x		x
Li_2PS_3	2.500	17.5		x /√		√
LiP_5	1.208	19.3		x		
Li_7PS_6	2.080	17.8		x		
$LiCl$	5.926	21.2			x	x
SCl	2.890	35.2			√	
PCl_3	4.076	36.9			√	
SCl_4	2.618	30.3				√

*The bandgap of P_2S (0 eV) is obtained from Materials project, which might be different from the experimental case. However, its low composition in Table S1-S3 does not change the result qualitatively if the bandgap is any nonzero value.

Table S5. Ionic conductivity values obtained either experimentally or computationally for sulfide-based SEs with different chlorine content**.**

Compound	Experimental/Computational methodology	Conductivity value (mS cm^{-1})	Reference
Li_3PS_4	SSR+Crystallization	$3 \cdot 10^{-4}$ (γ-phase)	[8]
	SSR+Crystallization	$3 \cdot 10^{-4}$ (γ-phase, RT)/30 (β-phase, 227ºC)	[9]
	Solution based synthesis	$2.3 \cdot 10^{-3}$ (RT)	[10]
	Solution based synthesis	0.2 (Nanoporous β-phase, RT)	[11]
$Li_7P_3S_{11}$	Solution based synthesis	~0.1	[12]
	Crystallization from the melt $70Li_2S \cdot 30P_2S_5$	2.9	[13]
	Crystallization from the melt $70Li_2S \cdot 30P_2S_5$	3.2 (cold-pressed)/17 (hot-sintered)	[14]
	Solvent-assisted ball milling	0.1	[15]
Li_7PS_6	SSR	LT-$1.6 \cdot 10^{-3}$ (40ºC)/HT-$5.9 \cdot 10^{-2}$ (227ºC)	[16]
	SSR	$8 \cdot 10^{-2}$ (RT)	[17]
	Solution based synthesis	0.1	[18]
$Li_{6.25}PS_{5.25}Cl_{0.75}$	Ball milling+annealing	1.03	[19]
Li_6PS_5Cl	Mechanochemical Milling	1.33	[20]
	Mechanical Milling	0.1	[21]
	Solution based synthesis	$1.4 \cdot 10^{-2}$	[22]
	Solution based synthesis	$6 \cdot 10^{-2}$	[23]
	Solution based synthesis	2.4	[24]
	Solid-State reaction	4.96 (26.2ºC)	[25]
	Solid-State reaction	3.15	[26]
$Li_{5.5}PS_{4.5}Cl_{1.5}$	Solution based synthesis	3.9	[24]
	Ball milling+SSR	6.4	[27]
	Ball milling+SSR	9.4	[28]
	High energy ball milling+ultrafast annealing	10.2	[29]
$Li_5PS_4Cl_2$	DFT MD (computational)	150	[30]
	AIMD	1.85	[31]
	bond valence site energy (BVSE)	$3 \cdot 10^{-7}$	[32]

RT-Room Temperature, HT-High Temperature, LT-Low Temperature

Table S6. LPSCl-LCO and LPSCl-LNMO interface reaction products with fraction numbers within each voltage range at effective modulus K_{eff} = 20 GPa, which is a metric for the level of local mechanical constrictions.

Voltage (V)	LPSCl-$LiCoO_2$
5.0	$0.328Li + 0.3000CoS_2 + 0.095Li_6CoCl_8 + 0.317CoSO_4 + 0.282LiCo_2P_3O_{10} + 0.006Li_2CoS_2O_8$
4.9	$0.317Li + 0.303CoS_2 + 0.085Li_6CoCl_8 + 0.179CoSO_4 + 0.235LiCo_2P_3O_{10} + 0.122Li_2CoS_2O_8 + 0.076Co_2ClPO_4$
4.1	$0.312Li + 0.304CoS_2 + 0.080Li_6CoCl_8 + 0.117CoSO_4 + 0.213LiCo_2P_3O_{10} + 0.176Li_2CoS_2O_8 + 0.110Co_2ClPO_4$
4.0	$0.311Li + 0.304CoS_2 + 0.078Li_6CoCl_8 + 0.010CoP_2O_6 + 0.093CoSO_4 + 0.192LiCo_2P_3O_{10} + 0.197Li_2CoS_2O_8 + 0.126Co_2ClPO_4$
3.6	$0.307Li + 0.305CoS_2 + 0.069Li_6CoCl_8 + 0.049CoP_2O_6 + 0.111LiCo_2P_3O_{10} + 0.279Li_2CoS_2O_8 + 0.187Co_2ClPO_4$
3.5	$0.248Li + 0.130Co_9S_8 + 0.269CoS_2 + 0.296Li_3PO_4 + 0.101Li_6CoCl_8 + 0.189Li_2CoS_2O_8 + 0.015Co_2PClO_4$
3.4	$0.240Li + 0.042Co_9S_8 + 0.153CoS_2 + 0.208Co_3S_4 + 0.305Li_3PO_4 + 0.103Li_6CoCl_8 + 0.189Li_2CoS_2O_8$
2.8	$0.206Li + 0.067Co_9S_8 + 0.077CoS_2 + 0.276Co_3S_4 + 0.305Li_3PO_4 + 0.172Li_2SO_4 + 0.103Li_6CoCl_8$
2.7	$0.206Li + 0.067Co_9S_8 + 0.077CoS_2 + 0.276Co_3S_4 + 0.305Li_3PO_4 + 0.172Li_2SO_4 + 0.103Li_6CoCl_8$
2.5	$0.201Li + 0.022LiCl + 0.210Co_9S_8 + 0.212CoS_2 + 0.305Li_3PO_4 + 0.172Li_2SO_4 + 0.079Li_6CoCl_8$

Voltage (V)	LPSCl-$LiNi_{0.5}Mn_{1.5}O_4$
5.0	$0.291Li + 0.091NiCl_2 + 0.153Ni_3S_4 + 0.227NiS + 0.178NiSO_4 + 0.014LiNiP_3O_9 + 0.337Mn_5ClP_3O_{12}$
4.6	$0.253Li + 0.091NiCl_2 + 0.060Ni_3S_4 + 0.334NiS + 0.018\ NiSO_4 + 0.014LiNiP_3O_9 + 0.147Li_2NiS_2O_8 + 0.336Mn_5ClP_3O_{12}$
4.4	$0.253Li + 0.094NiCl_2 + 0.049Ni_3S_4 + 0.345NiS + 0.044Mn_2P_2O_7 + 0.161Li_2NiS_2O_8 + 0.004\ NiSO_4 + 0.303Mn_5ClP_3O_{12}$
4.0	$0.253Li + 0.094NiCl_2 + 0.046Ni_3S_4 + 0.349NiS + 0.048Mn_2P_2O_7 + 0.162Li_2NiS_2O_8 + 0.003\ MnSO_4 + 0.298Mn_5ClP_3O_{12}$
3.9	$0.1978Li + 0.1406NiS_2 + 0.2418Mn_2S_3 + 0.1078S_8O + 0.1394Li_3PO_4 + 0.0411Li_2S_2O_7 + 0.3293LiMn_2P_3O_{10}$
3.7	$0.1931Li + 0.1406NiS_2 + 0.2403Mn_2S_3 + 0.1099S_8O + 0.1350Li_3PO_4 + 0.0404Li_2SO_4 + 0.3338LiMn_2P_3O_{10}$
3.6	$0.1838Li + 0.1406NiS_2 + 0.2194Mn_2S_3 + 0.1298S_8O + 0.2044Li_3PO_4 + 0.0150Li_2SO_4 + 0.2908Mn_2P_2O_7$
3.5	$0.1865Li + 0.1406NiS_2 + 0.2236Mn_2S_3 + 0.1256S_8O + 0.1926Li_3PO_4 + 0.0113Li_2SO_4 + 0.2053Mn_2P_2O_7 + 0.0115MnSO_4 + 0.0895LiMn_2P_3O_{10}$
3.4	$0.1839Li + 0.1406NiS_2 + 0.2194Mn_2S_3 + 0.1298S_8O + 0.2044Li_3PO_4 + 0.0150Li_2SO_4 + 0.2908Mn_2P_2O_7$
3.3	$0.1783Li + 0.1406NiS_2 + 0.2125Mn_2S_3 + 0.1368S_8O + 0.1907Li_3PO_4 + 0.0045Li_2SO_4 + 0.2070Mn_2P_2O_7 + 0.1079LiMnPO_4$
3.2	$0.1759Li + 0.1406NiS_2 + 0.2096Mn_2S_3 + 0.1398S_8O + 0.1848Li_3PO_4 + 0.1708Mn_2P_2O_7 + 0.1544LiMnPO_4$
3.1	$0.1738Li + 0.1406NiS_2 + 0.2117Mn_2S_3 + 0.1384S_8O + 0.1891Li_3PO_4 + 0.1691Mn_2P_2O_7 + 0.1511LiMnPO_4$
3.0	$0.0731Li + 0.1406NiS_2 + 0.3623MnS_2 + 0.0095S_8O + 0.3695Li_3PO_4 + 0.0116Mn_2P_2O_7 + 0.1065LiMnPO_4$

2.8	$0.0728Li + 0.1406NiS_2 + 0.3627MnS_2 + 0.0092S_8O + 0.3650Li_3PO_4 + 0.1122LiMnPO_4 + 0.0103Li_2MnP_2O_7$
2.5	$0.0313Li + 0.1094Ni_3S_4 + 0.4219MnS_2 + 0.4687Li_3PO_4$

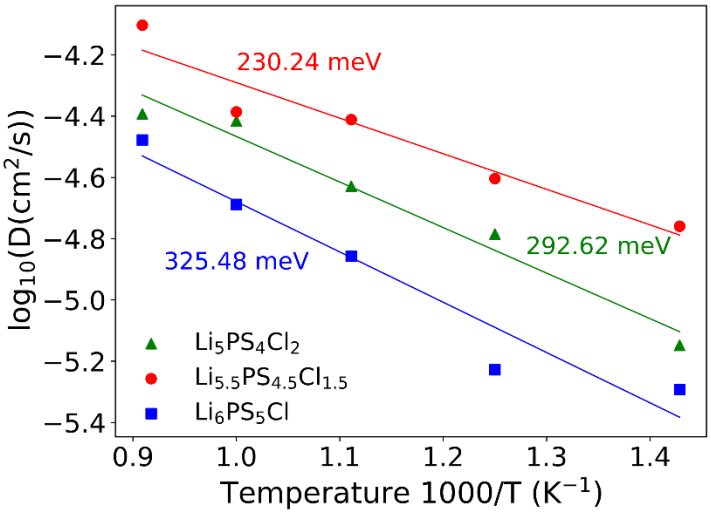

Figure S3. Arrhenius plots of $Li_{7-x}PS_{6-x}Cl_x$ (x=1.0, 1.5 and 2.0) from AIMD simulations.

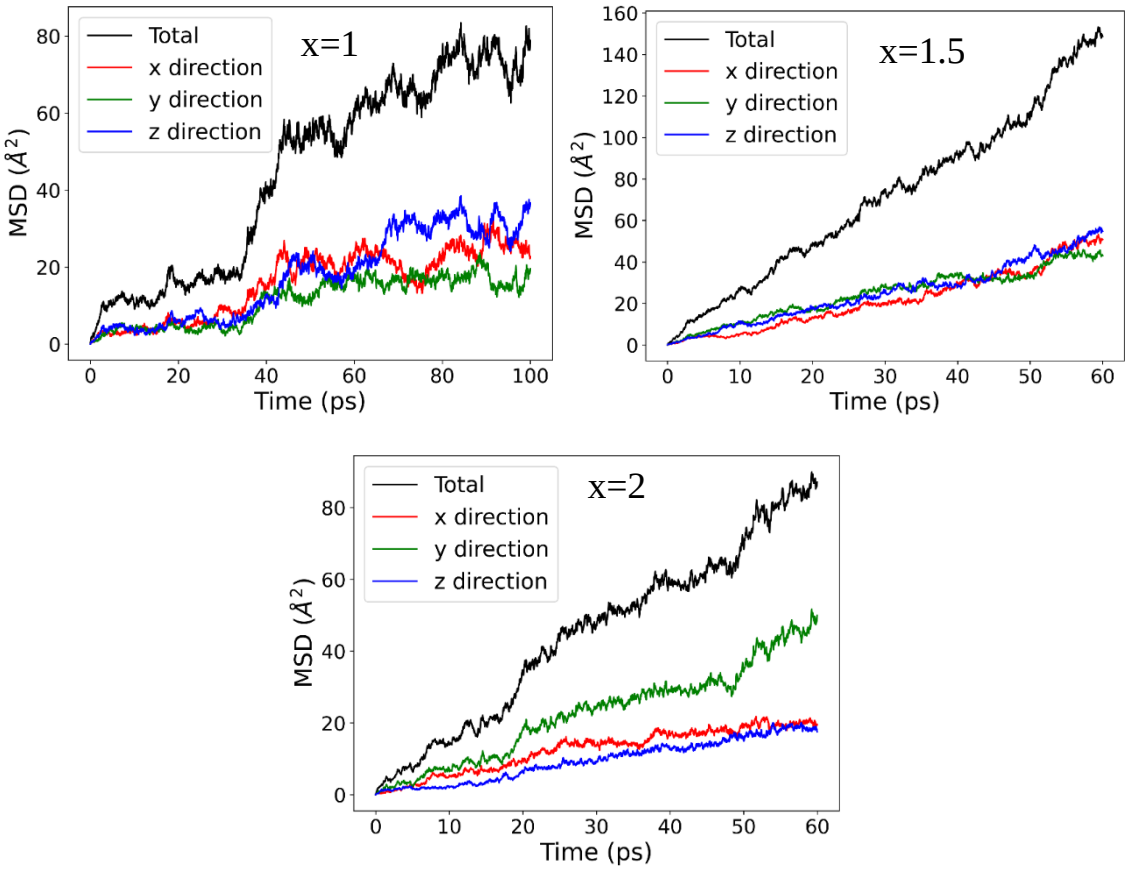

Figure S4. Mean square displacement (MSD) of Li ion for $Li_{7-x}PS_{6-x}Cl_x$ (x=1.0, 1.5 and 2.0) from 900 K AIMD simulations.

$Li_{5.5}PS_{4.5}Cl_{1.5}$ (LPSCl) and $Li_7P_3S_{11}$ (LPS) synthesis and characterization

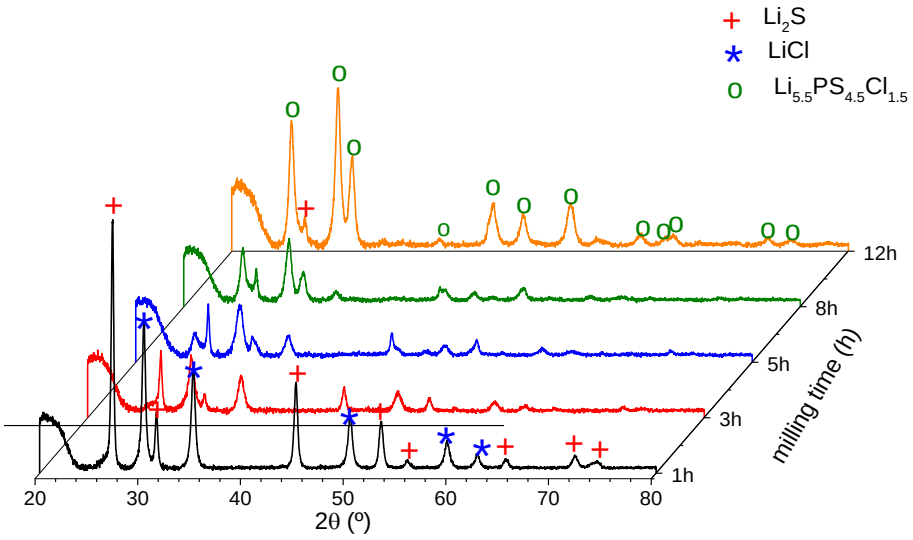

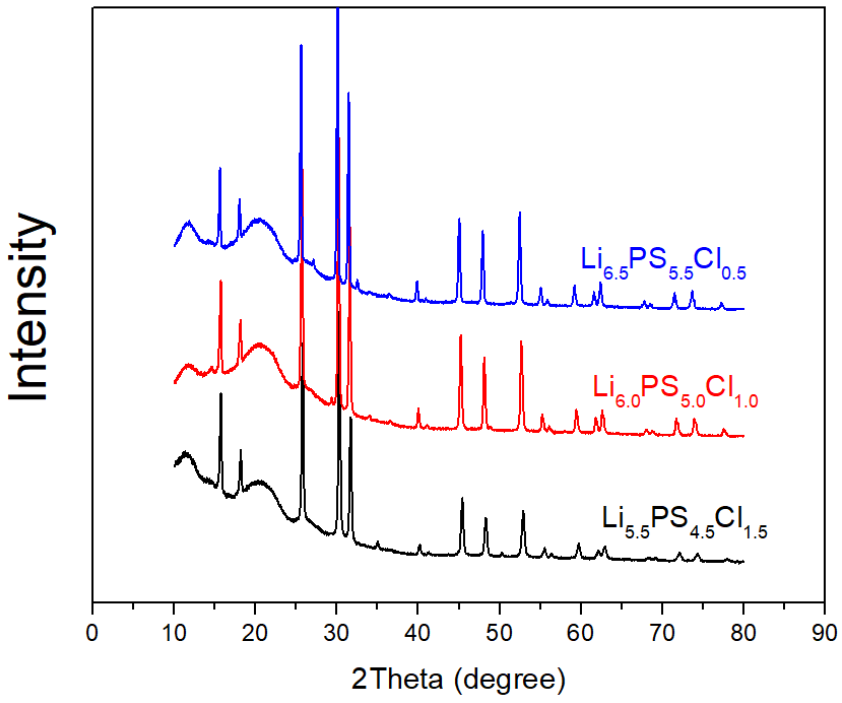

Figure S5. (a) Waterfall plot of XRD patterns showing the in-situ crystallization of $L_{5.5}PS_{4.5}Cl_{1.5}$ as a function of time, after milling stoichiometric amounts of Li_2S, P_2S_5 and LiCl. (b) XRD patterns of $L_{6-x}PS_{5-x}Cl_{1+x}$ (x=±0.5 and 0) after annealing for 8 hours.

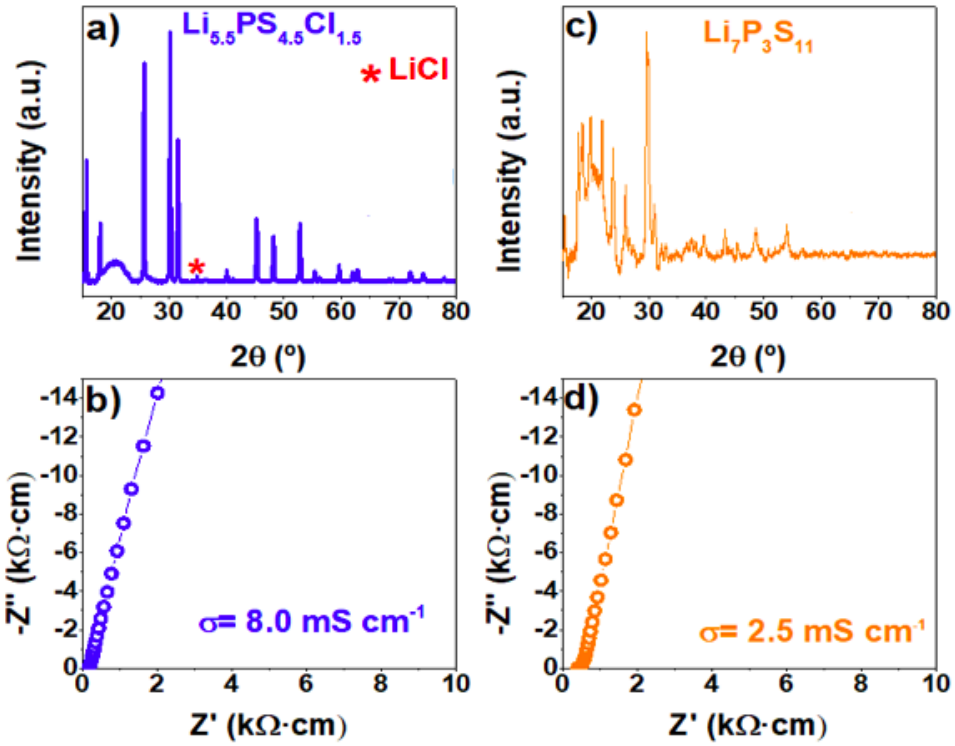

Figure S6. Powder XRD pattern and impedance complex plot at room temperature (22 ºC) of $L_{5.5}PS_{4.5}Cl_{1.5}$ (a) and (b), and $Li_7P_3S_{11}$ (c) and (d).

$Li_{5.5}PS_{4.5}Cl_{1.5}$ (LPSCl) and $Li_7P_3S_{11}$ (LPS)-Li metal chemical stability

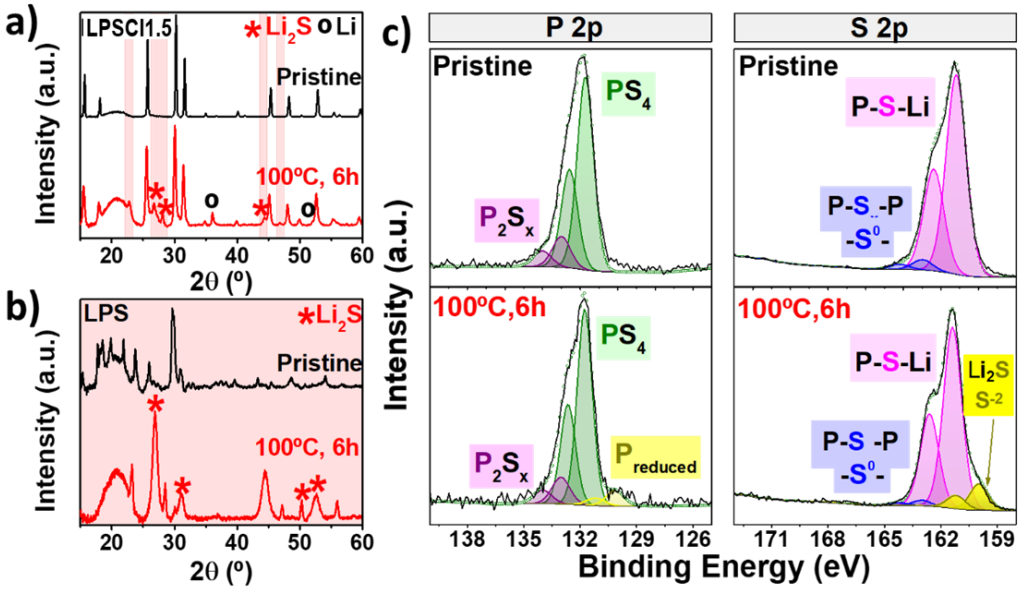

Figure S7. XRD patterns of a mixture of a) LPSCl1.5 and b) LPS with Li metal powder (70:30-SE:Limetal powder) heated at 100 ºC for 6 h (100 ºC, 6h). c) Ex-situ P 2p and S 2p XPS spectra of LPSCl1.5 after the heat treatment with Li powders (100ºC, 6h). For comparison purposes, XRD patterns of pristine LPSCl and LPS have been included in a) and b), respectively, as well as the P 2p and S 2p XPS spectra of pristine LPSCl1.5 in c).

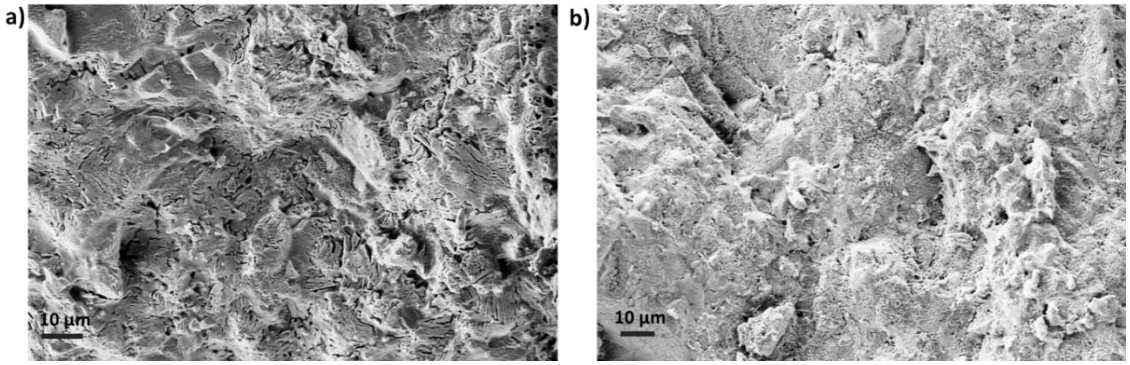

Figure S8. Scanning electron microscopy (SEM) images of LPSCl1.5 (a) and LPSCl1.0 (b) regions after cycling at 0.25mA/cm^2 for 100 hours. For (a) the battery is constructed with the multilayer structure of Li/G-LPSCl1.5-LPSCl1.0-LPSCl1.5-G/Li, and the SEM image is taken from the cross section of the LPSCl1.5 layer. For (b) the battery is constructed with the structure of Li/G-LPSCl1.0-G/Li, and the SEM image is taken from the cross section of the LPSCl1.0 layer at around the same relative distance to Li/G anode as where we took SEM in (a).

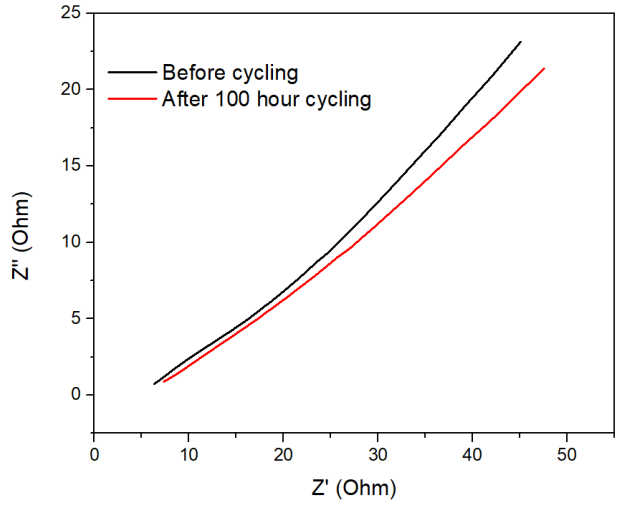

Figure S9. Impedance of the battery before and after at 0.25mA/cm^2 for 100 hours. The battery is constructed with the structure of Li/G-LPSCl1.5-LPSCl1.0-LPSCl1.5-G/Li.

Cyclic Voltammograms tests

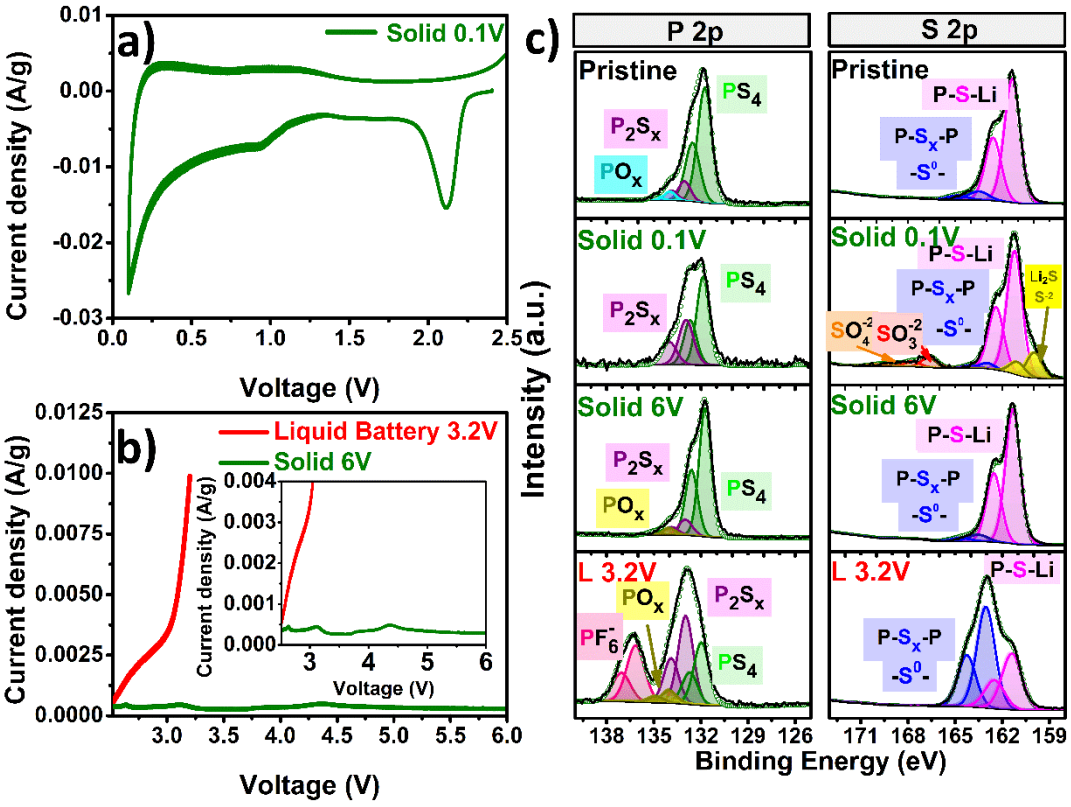

Figure S10. Cyclic voltammograms (CV) from OCV to 0.1 V a) and to 6 V b). c) Ex-situ P 2p and S 2p XPS spectra of constrained LPSCl in a Li/LPSCl1.5/(LPSCl1.5+C) cell from OCV to 0.1 V (Solid 0.1V) and to 6 V (Solid 6V) and Li/1M $LiPF_6$ in EC-DMC/(LPSCl1.5+C) cells from OCV to 3.2 V (L 3.2V).

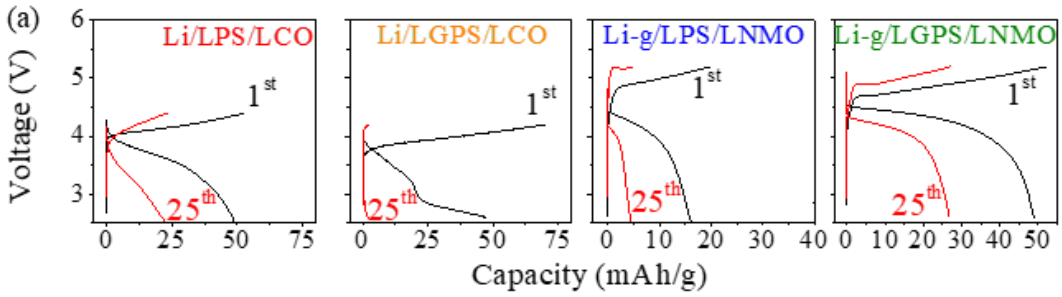

Figure S11. (a) Galvanostatic charge-discharge voltage profiles of Li/SE/LCO, Li-G/SE/LNMO (SE is LPS or LGPS).

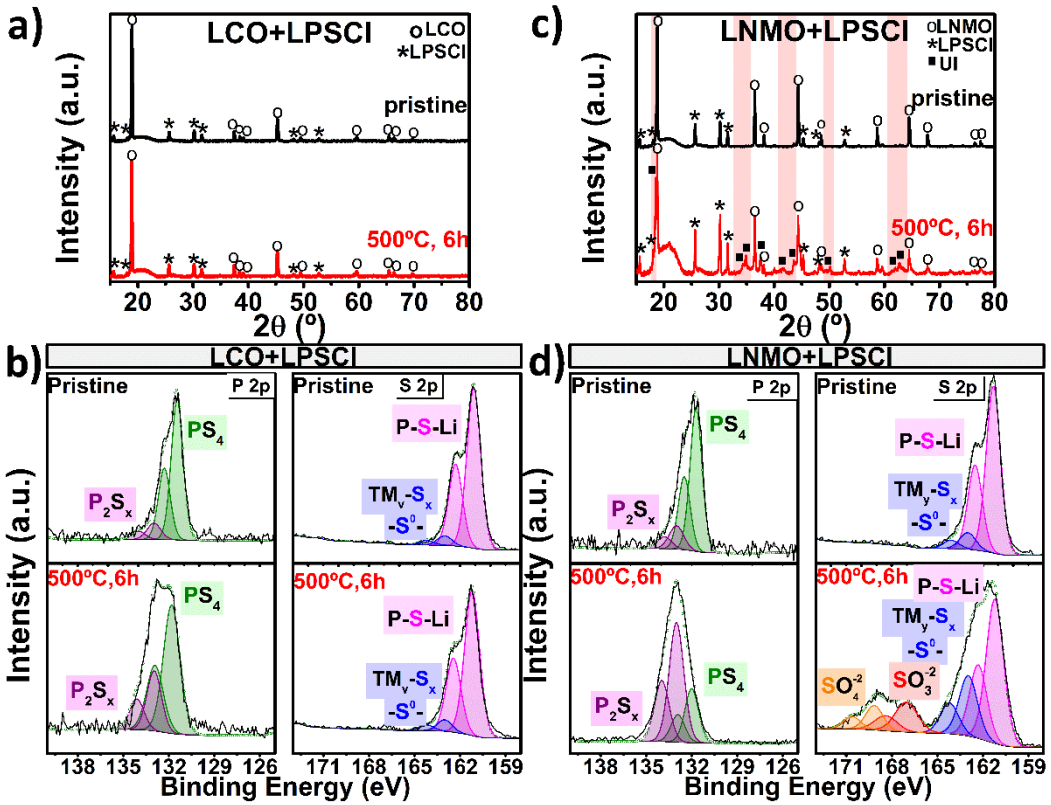

Figure S12. XRD patterns and ex-situ P 2p and S 2p XPS spectra of 0.7LPSCl1.5-0.3LCO (w/w) (a, b) and 0.7LPSCl1.5-0.3LNMO (w/w) (c, d) composites before (pristine) and after a heat treatment at 500ºC for 6 hours (500ºC, 6h).

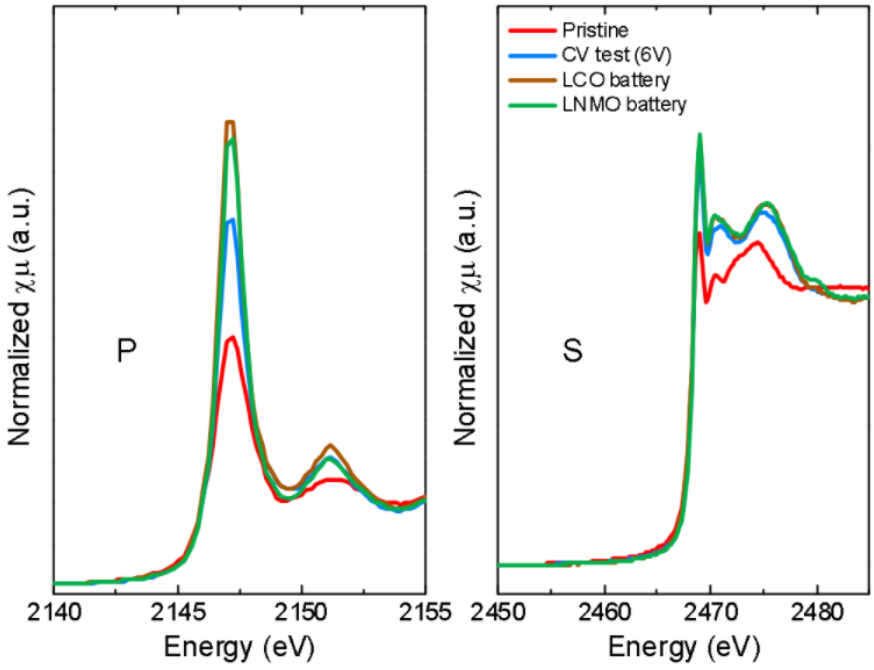

Figure S13. XAS spectra of LPSCl1.5 before (red) and after cycling with LCO (brown), LNMO (green) and after CV measurement at 6V (blue): (a) P K-edge and (b) S K-edge.

References

1. Ye, L. *et al.* Toward Higher Voltage Solid-State Batteries by Metastability and Kinetic Stability Design. *Adv. Energy Mater.* **2001569**, 1–13 (2020).

2. Su, Y. *et al.* A more stable lithium anode by mechanical constriction for solid state batteries. *Energy Environ. Sci.* (2020). doi:10.1039/c9ee04007b

3. Kohn, W. & Sham, L. J. Self-Consistent Equations Including Exchange and Correlation Effects. *Phys. Rev.* **140**, A1133–A1138 (1965).

4. Hoover, W. G. Canonical dynamics: Equilibrium phase-space distributions. *Phys. Rev. A* **31**, 1695–1697 (1985).

5. He, X., Zhu, Y., Epstein, A. & Mo, Y. Statistical variances of diffusional properties from ab initio molecular dynamics simulations. *npj Comput. Mater.* **4**, 18 (2018).

6. Fitzhugh, W., Wu, F., Ye, L., Su, H. & Li, X. Strain-Stabilized Ceramic-Sulfide Electrolytes. *Small* **1901470**, 1–14 (2019).

7. Powell, M. J. Site percolation in randomly packed spheres. *Phys. Rev. B* **20**, 4194–4198 (1979).

8. Tachez, M., Malugani, J.-P., Mercier, R. & Robert, G. Ionic conductivity of and phase transition in lithium thiophosphate Li_3PS_4. *Solid State Ionics* **14**, 181–185 (1984).

9. Homma, K. *et al.* Crystal structure and phase transitions of the lithium ionic conductor Li_3PS_4. *Solid State Ionics* **182**, 53–58 (2011).

10. Teragawa, S., Aso, K., Tadanaga, K., Hayashi, A. & Tatsumisago, M. Liquid-phase synthesis of a Li_3PS_4 solid electrolyte using N-methylformamide for all-solid-state lithium batteries. *J. Mater. Chem. A* **2**, 5095–5099 (2014).

11. Liu, Z. *et al.* Anomalous High Ionic Conductivity of Nanoporous β-Li_3PS_4. *J. Am. Chem. Soc.* **135**, 975–978 (2013).

12. Fan, B. *et al.* Influence of precipitate/supernatant ratio during liquid-phase synthesis of solid electrolyte $Li_7P_3S_{11}$. *Solid State Ionics* **343**, 115073 (2019).

13. Minami, K., Hayashi, A. & Tatsumisago, M. Preparation and characterization of superionic conducting $Li_7P_3S_{11}$ crystal from glassy liquids. *J. Ceram. Soc. Japan* **118**, 305–308 (2010).

14. Seino, Y., Ota, T., Takada, K., Hayashi, A. & Tatsumisago, M. A sulphide lithium super ion conductor is superior to liquid ion conductors for use in rechargeable batteries. *Energy Environ. Sci.* **7**, 627–631 (2014).

15. Xue, B. *et al.* Solvent-assisted ball milling for synthesizing solid electrolyte $Li_7P_3S_{11}$. *J. Am. Ceram. Soc.* **102**, 3402–3410 (2019).

16. Deiseroth, H.-J. *et al.* Li_7PS_6 and Li_6PS_5X (X: Cl, Br, I): Possible Three-dimensional Diffusion Pathways for Lithium Ions and Temperature Dependence of the Ionic Conductivity by Impedance Measurements. *Zeitschrift für Anorg. und Allg. Chemie* **637**, 1287–1294 (2011).

17. Hayashi, A., Hama, S., Morimoto, H., Tatsumisago, M. & Minami, T. High Lithium Ion Conductivity of Glass–Ceramics Derived from Mechanically Milled Glassy Powders. *Chem. Lett.* **30**, 872–873 (2001).

18. Ziolkowska, D. A., Arnold, W., Druffel, T., Sunkara, M. & Wang, H. Rapid and

Economic Synthesis of a Li_7PS_6 Solid Electrolyte from a Liquid Approach. *ACS Appl. Mater. Interfaces* **11**, 6015–6021 (2019).

19. Xuan, M. *et al.* Ultrafast solid-state lithium ion conductor through alloying induced lattice softening of Li_6PS_5Cl. *J. Mater. Chem. A* **6**, 19231–19240 (2018).

20. Boulineau, S., Courty, M., Tarascon, J.-M. & Viallet, V. Mechanochemical synthesis of Li-argyrodite Li_6PS_5X (X=Cl, Br, I) as sulfur-based solid electrolytes for all solid state batteries application. *Solid State Ionics* **221**, 1–5 (2012).

21. Rao, R. P. & Adams, S. Studies of lithium argyrodite solid electrolytes for all-solid-state batteries. *Phys. status solidi* **208**, 1804–1807 (2011).

22. Yubuchi, S. *et al.* Preparation of high lithium-ion conducting Li_6PS_5Cl solid electrolyte from ethanol solution for all-solid-state lithium batteries. *J. Power Sources* **293**, 941–945 (2015).

23. Rosero-Navarro, N. C., Miura, A. & Tadanaga, K. Preparation of lithium ion conductive Li_6PS_5Cl solid electrolyte from solution for the fabrication of composite cathode of all-solid-state lithium battery. *J. Sol-Gel Sci. Technol.* **89**, 303–309 (2019).

24. Zhou, L. *et al.* Solvent-Engineered Design of Argyrodite Li_6PS_5X (X = Cl, Br, I) Solid Electrolytes with High Ionic Conductivity. *ACS Energy Lett.* **4**, 265–270 (2019).

25. Yu, C. *et al.* Facile Synthesis toward the Optimal Structure-Conductivity Characteristics of the Argyrodite Li_6PS_5Cl Solid-State Electrolyte. *ACS Appl. Mater. Interfaces* **10**, 33296–33306 (2018).

26. Wang, S. *et al.* High-Conductivity Argyrodite Li_6PS_5Cl Solid Electrolytes Prepared via Optimized Sintering Processes for All-Solid-State Lithium–Sulfur Batteries. *ACS Appl. Mater. Interfaces* **10**, 42279–42285 (2018).

27. Yu, C. *et al.* Superionic conductivity in lithium argyrodite solid-state electrolyte by controlled Cl-doping. *Nano Energy* **69**, 104396 (2020).

28. Adeli, P. *et al.* Boosting Solid-State Diffusivity and Conductivity in Lithium Superionic Argyrodites by Halide Substitution. *Angew. Chemie Int. Ed.* **58**, 8681–8686 (2019).

29. Jung, W. D. *et al.* Superionic Halogen-Rich Li-Argyrodites Using In Situ Nanocrystal Nucleation and Rapid Crystal Growth. *Nano Lett.* **20**, 2303–2309 (2020).

30. de Klerk, N. J. J., Rosłoń, I. & Wagemaker, M. Diffusion Mechanism of Li Argyrodite Solid Electrolytes for Li-Ion Batteries and Prediction of Optimized Halogen Doping: The Effect of Li Vacancies, Halogens, and Halogen Disorder. *Chem. Mater.* **28**, 7955–7963 (2016).

31. Zhu, Z., Chu, I.-H. & Ong, S. P. $Li_3Y(PS_4)_2$ and $Li_5PS_4Cl_2$: New Lithium Superionic Conductors Predicted from Silver Thiophosphates using Efficiently Tiered Ab Initio Molecular Dynamics Simulations. *Chem. Mater.* **29**, 2474–2484 (2017).

32. Prasada Rao, R., Chen, H. & Adams, S. Stable Lithium Ion Conducting Thiophosphate Solid Electrolytes $Li_x(PS_4)_yX_z$ (X = Cl, Br, I). *Chem. Mater.* **31**, 8649–8662 (2019).